

A MULTIPLY IMAGED LUMINOUS INFRARED GALAXY BEHIND THE BULLET CLUSTER (1E0657-56)*

ANTHONY H. GONZALEZ¹, DOUGLAS CLOWE², MARUŠA BRADAČ³, DENNIS ZARITSKY⁴, CHRISTINE JONES⁵, AND
 MAXIM MARKEVITCH⁵

¹ Department of Astronomy, University of Florida, Gainesville, FL 32611-2055, USA; anthony@astro.ufl.edu

² Department of Physics & Astronomy, Ohio University, Clippinger Labs 251B, Athens, OH 45701, USA

³ Department of Physics, University of California at Santa Barbara, Santa Barbara, CA 93106, USA

⁴ Steward Observatory, University of Arizona, 933 North Cherry Avenue, Tucson, AZ 85721, USA

⁵ Harvard-Smithsonian Center for Astrophysics, 60 Garden St., Cambridge, MA 02138, USA

Received 2008 April 2; accepted 2008 September 22; published 2009 January 15

ABSTRACT

We present evidence for a *Spitzer*-selected luminous infrared galaxy (LIRG) behind the Bullet Cluster (1E0657-56). The galaxy, originally identified as a multiply imaged source using Infrared Array Camera (IRAC) photometry, has a spectral energy distribution consistent with a highly extinguished ($A_V \sim 3.3$), strongly star forming galaxy at $z = 2.7$. Using our strong gravitational lensing model presented in a previous paper, we find that the magnifications are $|\mu| \approx 10$ –50 for the three images of the galaxy. The brightest and faintest images differ by a factor of 3.2 in magnification. The implied infrared luminosity is consistent with the galaxy being a LIRG, with a stellar mass of $M_* \sim 2 \times 10^{10} M_\odot$ and a star formation rate (SFR) of $\sim 90 M_\odot \text{ yr}^{-1}$. With lensed fluxes at 24 μm of 0.58 mJy and 0.39 mJy in the two brightest images, this galaxy presents a unique opportunity for detailed study of an obscured starburst with a SFR comparable to that of L^* galaxies at $z > 2$.

Key words: galaxies: clusters: general – galaxies: evolution – galaxies: starburst – gravitational lensing

Online-only material: color figure

1. INTRODUCTION

Measurements of both the star formation history of the universe and corollary buildup of stellar mass have established that the star formation rate (SFR) peaks at $1 \lesssim z \lesssim 3$ (e.g., Madau et al. 1996; Lilly et al. 1996; Dickinson et al. 2003; Rudnick et al. 2003; Reddy et al. 2008; Wilkins et al. 2008). *Spitzer* 24 μm observations further indicate that star formation at this epoch is dominated by luminous and ultraluminous infrared galaxies (LIRGs and ULIRGs; Pérez-González et al. 2005; Le Floc’h et al. 2005). ULIRGs are sufficiently bright to facilitate spectroscopy and detailed analyses (Daddi et al. 2005; Yan et al. 2005; Valiante et al. 2007; Pope et al. 2008); however, these galaxies represent only the most massive tail of the galaxy population (Dey et al. 2008; Dye et al. 2008).

In contrast, LIRGs have properties more similar to the overall galaxy population, with stellar masses and SFRs comparable to those seen for UV-selected star forming galaxies at $z \sim 2$ (Reddy & Steidel 2004; Reddy et al. 2006). The intrinsic faintness of LIRGs however precludes both high-fidelity multiwavelength photometry and spectroscopic programs at optical and infrared wavelengths at $z \gtrsim 2$.

Strong gravitational lensing enables observations of intrinsically fainter galaxies than is otherwise possible, and several recent programs have begun to exploit lensing by galaxy clusters to probe the properties of infrared (IR) and submillimeter luminous galaxies (e.g., Knudsen et al. 2008; Rigby et al. 2008, and references therein). The main limitation of this approach is simply the small number of known lensed galaxies that are luminous at these wavelengths.

In this paper, we present evidence for a strongly lensed LIRG that is triply imaged by the Bullet Cluster. This galaxy is the

only strongly lensed source for which the initial detection was made with *Spitzer* at mid-IR wavelengths, and due to its large magnification provides a window onto the properties of lower luminosity infrared galaxies than have previously been studied in this redshift regime. In previous papers our team has explored the physical properties of the Bullet Cluster, 1E0657-56, measuring its matter distribution and the properties of the X-ray gas (Markevitch et al. 2002, 2004; Clowe et al. 2004, 2006; Bradač et al. 2006), and constraining the dark matter self-interaction cross-section (Markevitch et al. 2004; Randall et al. 2008). The object that is the subject of this paper was first identified as a doubly lensed source in one of these papers (Bradač et al. 2006, Section 6 and Figure 8), and is independently detected as a millimeter source (Wilson et al. 2008a). Here we incorporate new *Hubble Space Telescope* (*HST*), *Spitzer Space Telescope*, and *Magellan* data in a detailed analysis of this object. The data are presented in Section 2, and are used in Section 3 to estimate the redshift, magnification, stellar mass, and SFR. In this section we also present evidence for a newly discovered, third image of this galaxy. We summarize our results in Section 2.

2. PHOTOMETRIC DATA AND MEASUREMENTS

We use the combination of the *Spitzer* Infrared Array Camera (IRAC; Fazio et al. 2004), the Multiband Imaging Photometer for *Spitzer* (MIPS; Rieke et al. 2004), *HST* Advanced Camera for Surveys (ACS; Ford et al. 2003), and ground-based near-infrared (NIR) observations to constrain the spectral energy distribution of the multiply imaged source. The subsections below describe the data and photometric analysis associated with each facility.

2.1. *Spitzer* IRAC

We originally detected this source as a doubly imaged object in *Spitzer* IRAC data obtained on 2004 December 17–18. The data from this program include imaging in all four IRAC bands

* This paper includes data gathered with the 6.5 m *Magellan* Telescopes located at Las Campanas Observatory, Chile, the *Hubble Space Telescope*, and the *Spitzer Space Telescope*.

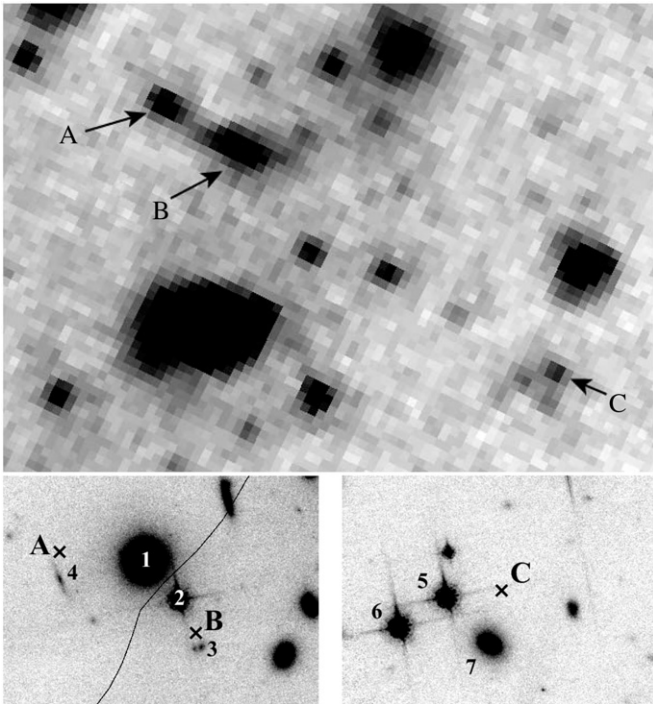


Figure 1. Top: 8 μm image showing the location of image C relative to images A and B. In this image the galaxy between images A and B has been subtracted for clarity. The field of view (FOV) is $65'' \times 50''$. Bottom: F850LP cutouts of the regions surrounding lensed images A and B (left) and image C (right). The crosses denote the locations of each image; the solid curve in the left panel is the critical curve from the $z = 2.7$ magnification map. The objects detected in the F850LP image that lie closest to the IRAC coordinates for images A and B are numbered 1–4. Object 1 is a cluster elliptical galaxy and object 2 is a star. The two fainter galaxies (3 and 4) are offset from the IRAC detections by $0''.8$ and $1''.5$, whereas the relative astrometry is good to $0''.25$, and can thus be excluded as optical counterparts to the lenses. The FOV is $17'' \times 12''$ in both panels. For all images north is up and east is to the left.

(3.6 μm , 4.5 μm , 5.8 μm , and 8 μm). These data were taken with a cycling dither pattern with medium scale factor and 100 s frame time during an 8720 s duration Astronomical Observation Request (AOR). The effective exposure times are 4 ks in each filter.

We process the data using MOPEX (Makovoz et al. 2006), with a final pixel scale of $0''.86$. Before measuring aperture fluxes, we first use GALFIT (Peng et al. 2002) to model and subtract a cluster elliptical that lies directly between the two lensed images (object #1 in Figure 1), using a nearby isolated star as the input point-spread function (PSF) for GALFIT. The structural parameters for the galaxy are held fixed to values derived using the ACS data (see below), with only the position and magnitude permitted to vary.⁶ There is also a star between the two lensed images (object #2 in Figure 1) that is detected at 3.6 μm and 4.5 μm , but is fainter at these wavelengths than the lensed images. Due to its faintness, we mask this star rather than model it with GALFIT. We also mask two other nearby sources that lie within the background apertures (#3 and #4 in Figure 1).

We then perform aperture photometry using an aperture of radius $2''.4$ with a background annulus extending from $2''.4$ – $7''.2$, applying the point source aperture corrections given in the IRAC Data Handbook.⁷ We note that the total magnitude may be

underestimated by $\sim 10\%$ due to the modest spatial extension of the source in the IRAC data, but apply no additional correction for this factor. We measure the flux in an ensemble of off-source apertures to compute the photometric uncertainties. The resultant photometry is given in Table 1 for these two images, which we denote as A and B (Figure 1 and 2). Image B is brighter than A by a factor of 1.5, with consistent flux ratios in all bands (Figure 3), as required for a multiply imaged source. The coordinates are $(\alpha_{2000}, \delta_{2000}) = (06:58:38.0, -55:57:02)$ for image A and $(\alpha_{2000}, \delta_{2000}) = (06:58:37.1, -55:57:06)$ for image B.

In Table 1 we also present photometry for a newly discovered third image of the galaxy, hereafter denoted as image C (see Figure 1), which is discussed in greater detail in Section 3.2. The IRAC photometry for image C is obtained in the same fashion as for images A and B, in this case modelling and subtracting two nearby stars and one nearby galaxy (objects #5–7 in Figure 1).

2.2. *Spitzer MIPS*

The MIPS 24 μm data were acquired on 2007 November 30. Observations were taken in small-scale photometry mode using a 3×3 raster map with each position offset by half the array. The frame time for individual exposures is 30 s.

We process the data using MOPEX, with a final pixel scale of $1''.22$. At this wavelength images A, B, and C are all clearly detected. We use Astronomical Point source EXtractor (APEX; Makovoz et al. 2002; Makovoz & Marleau 2005) to perform point source photometry, deblending images A and B. The fluxes of all three lensed images, which are derived via PSF fitting, are reported in Table 1. The quoted uncertainties include uncertainty associated with background subtraction, which dominate over the statistical uncertainties reported by APEX. The MIPS point source photometry does not suffer from contamination by foreground sources. The spectral energy distributions of cluster ellipticals fall rapidly between 8 μm and 24 μm and the nearby sources modelled at shorter wavelengths are not detected at 24 μm .

2.3. *HST ACS*

We observed the Bullet Cluster with the ACS through the F606W, F775W, and F850LP filters. The F606W data were taken on 2004 October 21, with a total exposure time of 4.7 ks. The F775W and F850LP data were taken on 2006 October 12–13, with total exposure times of 10.1 ks and 12.7 ks, respectively. All observations were reprocessed and drizzled to a common coordinate system using custom software (HAGGLEs; Marshall et al. 2009, in preparation) based upon MultiDrizzle (Koekemoer et al. 2002).

For the *HST* data we perform aperture photometry within $1''.5$ aperture radii. This aperture size is selected as a tradeoff between two competing factors. Specifically, while smaller apertures yield more stringent lower limits on the magnitude, the aperture size must be sufficiently large to encompass the total flux from each lensed image. Given that IRAC provides the highest resolution data in which the source is detected, our information about the true physical extent of the lensed images is limited. The galaxy shows only limited spatial extent at 3.6 μm , indicating that a $1''.5$ aperture is sufficiently large to enclose the total flux in the ACS imaging. Any future higher resolution detection of this object will enable use of smaller apertures and yield improved magnitude limits. As with the IRAC data, we determine the photometric uncertainty using an ensemble of background apertures.

⁶ The position is permitted to vary at the subpixel level to minimize errors in the subtraction due to residual misregistration between the images. Fixing the position does not qualitatively alter our results.

⁷ See <http://ssc.spitzer.caltech.edu/irac/dh/>. A $2''.4$ aperture is the smallest for which corrections are given.

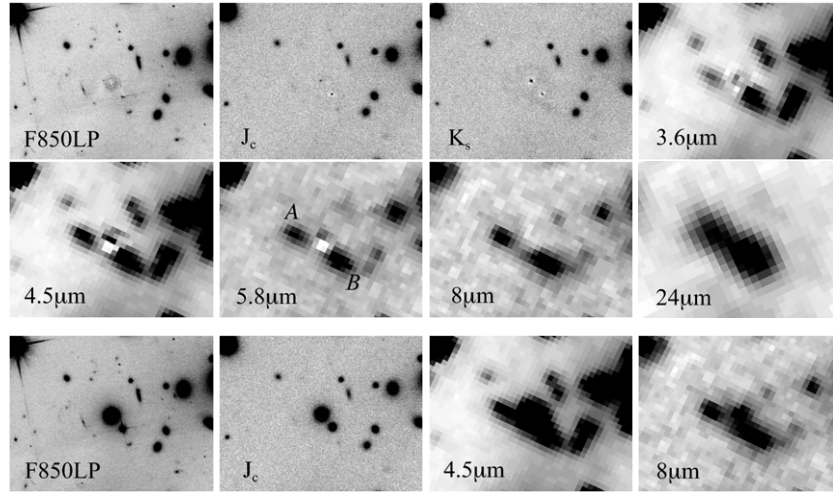


Figure 2. Cutout images of the region around the lensed galaxy, in order of increasing wavelength starting with the ACS F850LP data. In the first two rows we show the images used for the photometry after subtraction of contaminant sources using GALFIT. In the last row we show images prior to GALFIT subtraction for a representative sample of wavelengths (F850LP, J , $4.5\ \mu\text{m}$, and $8\ \mu\text{m}$). In all panels the FOV is $34'' \times 26''$. North is up and east is to the left.

Table 1
Observed Fluxes and Magnitudes for Lensed Images

| Passband | Image A | | Image B | | Image C | | Flux Ratios | |
|----------------------|-------------------------|------------------|-------------------------|------------------|-------------------------|------------------|-----------------|-----------------|
| | Flux (μJy) | Mag (AB) | Flux (μJy) | Mag (AB) | Flux (μJy) | Mag (AB) | B/A | B/C |
| F606W ^a | <0.29 | >25.26 | <0.29 | >25.26 | <0.29 | >25.26 | ... | ... |
| F775W | <0.24 | >24.67 | <0.24 | >24.67 | <0.24 | >24.67 | ... | ... |
| F850LP | <0.41 | >24.11 | <0.41 | >24.11 | <0.41 | >24.11 | ... | ... |
| J_c | <1.30 | >23.62 | <1.30 | >23.62 | <1.30 | >23.62 | ... | ... |
| K_s | <5.35 | >22.08 | <5.35 | >22.08 | <5.35 | >22.08 | ... | ... |
| $3.6\ \mu\text{m}^b$ | 13.6 ± 0.6 | 21.06 ± 0.05 | 21.0 ± 1.5 | 20.59 ± 0.08 | 7.4 ± 1.7 | 21.73 ± 0.25 | 1.54 ± 0.13 | 2.84 ± 0.68 |
| $4.5\ \mu\text{m}$ | 23.4 ± 0.9 | 20.47 ± 0.04 | 32.7 ± 1.5 | 20.11 ± 0.05 | 10.6 ± 1.7 | 21.34 ± 0.18 | 1.40 ± 0.08 | 3.08 ± 0.52 |
| $5.8\ \mu\text{m}$ | 38.4 ± 1.7 | 19.94 ± 0.05 | 57.9 ± 1.9 | 19.49 ± 0.03 | 16.8 ± 1.7 | 20.84 ± 0.11 | 1.51 ± 0.08 | 3.45 ± 0.37 |
| $8\ \mu\text{m}$ | 46.4 ± 2.5 | 19.73 ± 0.06 | 67.1 ± 2.5 | 19.33 ± 0.04 | 20.6 ± 2.5 | 20.62 ± 0.13 | 1.45 ± 0.09 | 3.25 ± 0.41 |
| $24\ \mu\text{m}$ | 390 ± 20 | 17.42 ± 0.05 | 575 ± 20 | $17.00 \pm .04$ | 175 ± 20 | 18.29 ± 0.12 | 1.47 ± 0.09 | 3.29 ± 0.39 |

Notes.

^a All quoted upper limits are 5σ confidence.

^b All IRAC photometry is calculated within $2\frac{1}{4}$ apertures and corrected to total magnitudes using the published point source aperture corrections. No additional correction has been applied to account for the extended nature of the source.

Before measuring aperture fluxes, we again use GALFIT to model and subtract contaminant sources near images A and B. In the *HST* imaging this includes objects #1 and #2. Near image C there are no objects that require subtraction for the *HST* data. We again use a nearby, isolated star as the input PSF for GALFIT, which has the advantage over TinyTim⁸ of correctly reproducing the red halo in F850LP (Gilliland & Riess 2002), and we recover consistent structural parameters for the cluster galaxy in all filters (effective radius $r_e = 0''.9$ and Sérsic index $n = 4.6$). We also mask out galaxy #3 in the aperture of image B (Figure 1). This galaxy cannot be the optical counterpart to the IRAC detection since it offsets from the IRAC detection by $0''.8$, whereas the relative astrometry is good to $0''.25$. Moreover, both the consistent flux ratios in all IRAC bands for images A and B (see Table 1 and Section 3) and the location of the critical curve in the lensing model support the interpretation that these are multiple images of the same source. In this case, the relative flux ratio of the two images should also be preserved in the *HST* data, and we would detect the counterimage in the other aperture at high confidence if it were the optical counterpart. For

Table 2
HST Photometry for Objects Near Lensed Images

| Figure 1 ID | F606W (AB) | F775W (AB) | F850LP (AB) | Object Type |
|-------------|------------------|------------------|------------------|-------------|
| 1 | 19.89 ± 0.02 | 19.05 ± 0.03 | 18.69 ± 0.03 | Galaxy |
| 2 | 19.79 ± 0.01 | 18.95 ± 0.01 | 19.17 ± 0.01 | Star |
| 3 | 24.27 ± 0.07 | 23.43 ± 0.07 | 23.39 ± 0.06 | Galaxy |
| 4 | 24.42 ± 0.07 | 23.58 ± 0.08 | 24.06 ± 0.08 | Galaxy |
| 5 | 20.34 ± 0.01 | 19.50 ± 0.01 | 18.75 ± 0.01 | Star |
| 6 | 19.81 ± 0.01 | 18.97 ± 0.01 | 18.60 ± 0.01 | Star |
| 7 | 21.27 ± 0.03 | 20.43 ± 0.03 | 20.18 ± 0.03 | Galaxy |

Notes. In this table we quote Source Extractor AUTO magnitudes. The uncertainties are calculated using artificial stars and galaxies.

completeness, in Table 2 we provide the *HST* photometry for the objects that are labelled in Figure 1, computed using Source Extractor.

2.4. Magellan PANIC

We imaged the central region of the Bullet Cluster with the PANIC instrument (Martini et al. 2004) on *Magellan* on

⁸ <http://www.stsci.edu/software/tinytim/tinytim.html>.

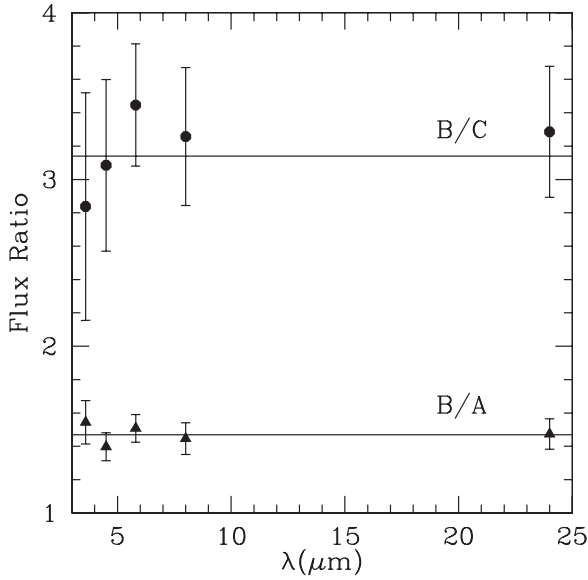


Figure 3. Flux ratios for the three images as a function of wavelength. The solid lines correspond to the weighted mean flux ratios, including data at all wavelengths. The observed flux ratios at different wavelengths are consistent to within the photometric uncertainties. For B/A (triangles) and B/C (circles) these mean values are 1.47 ± 0.06 and 3.18 ± 0.23 , respectively. The flux ratio for A/C, which is not plotted, is 2.16 ± 0.18 .

2006 March 06. Data were obtained in the J_c and K_s filters and photometrically calibrated to the Two Micron All Sky Survey (2MASS) point source catalog (Skrutskie et al. 2006), with seeing of $0''.55$ – $0''.6$ in both bands. Similar to the approach taken with the other data sets, we use GALFIT to fit and subtract off the bright galaxy and star that lie between the locations of images A and B in the IRAC data. We then measure the flux within the same $1''.5$ apertures employed for the ACS analysis, recovering only upper limits at the positions of all three images.

3. ANALYSIS

3.1. Spectral Energy Distribution and Photometric Redshift

In Figure 4 we plot the spectral energy distribution (SED) for each image of the lensed galaxy. Qualitatively, the combination of strong upper limits at optical and NIR wavelengths coupled with IRAC detections and a strong MIPS detection argue for the galaxy being a dusty starburst at $z \sim 2$, with the MIPS $24 \mu\text{m}$ emission being due to the redshifted polycyclic aromatic hydrocarbon (PAH) features. The $24 \mu\text{m}$ emission is difficult to explain if $z \gtrsim 3$, while the galaxy should be detected at NIR or optical wavelengths if either the internal extinction is low or the redshift is much below 2.

For a more quantitative answer, we use the photometric redshift code HyperZ (Bolzonella et al. 2000). The input spectral templates are obtained using the Charlot & Bruzual 2007 models (Bruzual 2007) with the Padova 1994 evolutionary tracks (Bertelli et al. 1994) and a Chabrier (2003) mass function. The templates are defined to have star formation histories identical to the default synthetic templates provided with HyperZ,⁹ and a Calzetti et al. (2000) extinction law is employed.

⁹ These templates have exponentially declining SFRs with $\tau = 1, 2, 3, 5, 15, 30$ Gyr for E, S0, Sa, Sb, Sc, and Sd galaxies, respectively. There is also a starburst template that corresponds to a single, instantaneous burst model. For all templates the metallicity is solar; however, Bolzonella et al. (2000) demonstrated that the redshift determination is not strongly dependent upon metallicity.

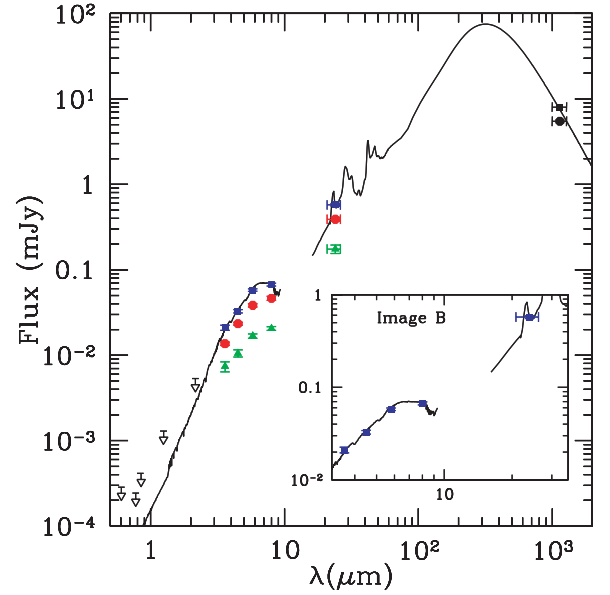


Figure 4. Spectral energy distribution for the galaxy. The solid points correspond to the observed fluxes for images A (circles), B (squares), and C (triangles), while the open arrows correspond to the 5σ upper limits at optical and NIR wavelengths. The solid circles at 1.1 mm are the AzTEC data from Wilson et al. (2008a, 2008b), where we have split their observed flux using the flux ratio derived for images A and B (see Figure 3). Horizontal error bars on the $24 \mu\text{m}$ data points denote the width of the filter, and for the AzTEC data correspond approximately to the system bandpass (Wilson et al. 2008b). The solid curve at $\lambda < 10 \mu\text{m}$ is the best-fit spectrum returned by HyperZ for image B, which corresponds to a starburst galaxy. The solid curve redward of $10 \mu\text{m}$ is the template from Chary & Elbaz (2001) that best fits the $24 \mu\text{m}$ flux for image A assuming $\mu_A = 25$. This template is redshifted to $z = 2.7$ and rescaled to image B using the observed flux ratio of the two images (Figure 3). Note that the AzTEC data, while not included in the fit, are fully consistent with this model. The inset zooms in on the wavelength regime covered by *Spitzer*, showing only the photometry for image B for clarity.

(A color version of this figure is available in the online journal.)

Since these stellar templates do not include PAH emission, for the photometric redshifts we fit only the data shortward of $10 \mu\text{m}$. HyperZ yields a best-fit redshift $z = 2.72^{+0.19}_{-0.32}$ for image A (90% confidence; $\chi^2_\nu = 0.5$). A small secondary peak in the redshift probability distribution is observed at $z = 5$ (Figure 5); however, this redshift is implausible because of the high observed flux at $24 \mu\text{m}$. An analysis of image B yields a similar redshift $z = 2.62^{+0.14}_{-0.22}$ ($\chi^2_\nu = 0.97$) with no secondary peak. In Bradač et al. (2006) we speculated that the source might be at $z > 6$, but this possibility is now excluded at high confidence ($\Delta\chi^2 > 8$). The best-fit spectral template (Figure 4) corresponds to a dusty starburst galaxy with $A_V = 3.3^{+2.2}_{-0.8}$ (90%) and an age of < 30 Myr. As can be seen in the figure, the robustness of the photometric redshift is largely due to the fact that the IRAC data span the $1.6 \mu\text{m}$ bump at this redshift.

At the best-fit redshift the $7.7 \mu\text{m}$ and $8.6 \mu\text{m}$ PAH features (blended in this spectrum) are redshifted beyond the $24 \mu\text{m}$ window, in which case the observed $24 \mu\text{m}$ emission is dominated by the $6.24 \mu\text{m}$ PAH feature. In a concurrent program Wilson et al. (2008a) have also identified this galaxy as a bright millimeter source, and obtain a consistent redshift ($z = 2.7$) via an empirical relation for SMGs between redshift and IRAC colors.

3.2. Magnification and Additional Images

The magnification map was obtained from the strong (information from multiply imaged systems) and weak (measuring

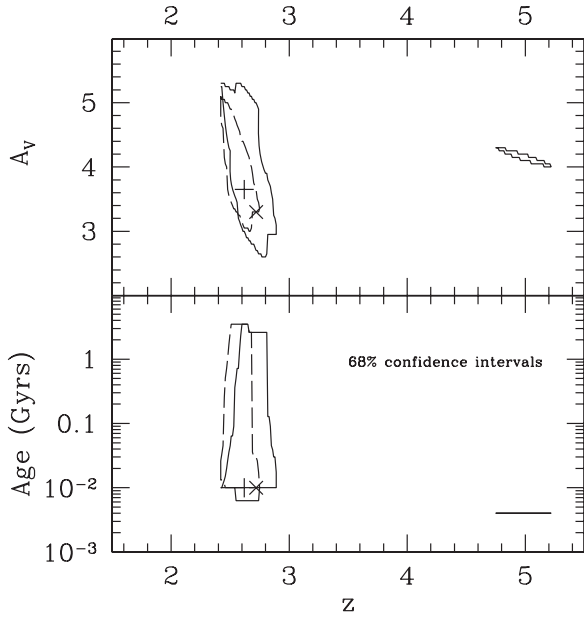


Figure 5. The 68% confidence intervals from HyperZ in the redshift–extinction and redshift–age planes. The solid curves denote the confidence intervals for image A; the dashed curves are for image B. The crosses (plus signs) denote the values corresponding to the minimum χ^2 for image A (B). There is a small secondary peak in the solutions for image A at $z = 5$.

distortion of background galaxies) gravitational lensing data. It is the same reconstruction as in Bradač et al. (2006). It is performed on a pixelized grid and does *not* assume a specific form of the underlying gravitational potential. At the location of image A we compute a magnification $|\mu| \sim 25$ and at image B we obtain $|\mu| \sim 50$ for a galaxy at $z = 2.7$. The critical curve (points of infinite magnification) passes between images A and B (see Figure 1)—their parity is reversed—supporting the hypothesis that A and B are indeed multiple images of the same source. These magnifications change by $< 20\%$ within the range of allowed photometric redshifts (90% confidence interval, see Section 3.1). The measured flux ratio of the two images is 1.47 ± 0.05 which is similar to the flux ratio of ~ 2 given by our lens model. In the subsequent discussion, we will quote the stellar mass and SFR in terms of $(\mu_A/25)^{-1}$ to reflect the inherent magnification uncertainty.

Given both lensing model and positions of images A and B, we can search for additional images of this source. We identified image C (Figure 1) at $(\alpha_{2000}, \delta_{2000}) = (06:58:33.4, -55:57:29)$ using the same initial lens model, which does not include information from images A and B of this object. The photometry for image C, described in Section 2, indicates that this image is a factor of 2.2 fainter than image A, while our lens model predicts a factor of 4. Given the uncertainties, these images are still consistent with being multiple images. The best-fit photometric redshift derived for this source is $z = 2.82^{+0.18}_{-0.20}$.

3.3. Stellar Mass

To estimate the stellar mass we use the code *kcorrect* (Blanton & Roweis 2007), which fits a linear combination of Bruzual & Charlot (2003) templates based upon Padova 1994 isochrones and spanning a range in metallicity (0.005–2.5 times solar) and age (1 Myr–13.75 Gyr). The required inputs are the photometric redshift from HyperZ and the IRAC photometry, reddening corrected using the A_V from HyperZ and the Calzetti et al. (2000) reddening law. In this analysis and Section 3.5 we

focus upon image A, but note that equivalent results hold for image B. For $z = 2.72$ and $A_V = 3.3$ we obtain a stellar mass $M_* = 1.5 \times 10^{10} (\mu_A/25)^{-1} M_\odot$.¹⁰ Thus, we find that this lensed galaxy is massive—similar in mass to LIRGs at lower redshift (Caputi et al. 2006).

3.4. Presence of Active Galactic Nuclei

In the sections above we have determined the redshift and stellar mass assuming that the observed SED is dominated by stars. It is true however that dusty starbursts and active galactic nuclei (AGN) are difficult to discriminate at the source redshift (e.g., see Barmby et al. 2006).

The simplest discriminator between the two contributors is spatial extent—any spatially extended emission must be stellar rather than due to an AGN. A visual inspection of Figure 2 demonstrates that the IRAC images do exhibit a modest extension perpendicular to the critical curve, arguing that the flux is not purely from an AGN. Next, we consider the *Chandra* observations to search for evidence of AGN activity. We find that the lensed source is a nondetection in our 500 ks exposure ($f < 3.6 \times 10^{-16}$ erg s $^{-1}$ cm $^{-2}$ unabsorbed, 3σ , for 0.5–2 keV). Comparing with the local X-ray to mid-IR relations of Krabbe et al. (2001), we find that a local Seyfert galaxy of comparable mid-IR luminosity should be more than a factor of 10 brighter than this limit, whereas nondetection is consistent with the expected relation for a starburst galaxy. While neither of the above arguments exclude an additional contribution from a central AGN, they do argue that we are not looking at a purely AGN spectrum.

Given the 24 μ m data, we can also consider whether this source, which is also a millimeter galaxy (Wilson et al. 2008a), has mid-IR colors consistent with a starburst or AGN. Comparing with the distribution of 24–8 μ m versus 8–4.5 μ m colors for SMGs in Pope et al. (2008), we find that the designation is ambiguous. The source lies close to, but outside the regime defined in Pope et al. (2008) for starburst galaxies, arguing that the observed SED may be a composite with AGN and starburst contributions.

3.5. Star Formation Rate

The only means of estimating the star formation rate with the existing data is via the strength of the PAH emission. There are two main caveats to this approach. First, any AGN contribution will bias our estimate of the SFR. Second, there exists large scatter in the relation between 8 μ m emission and star formation as traced by other methods (Calzetti 2008).

Keeping the above caveats in mind, we cautiously proceed with deriving a rough estimate of the SFR. To do so, we first convert the observed 24 μ m luminosity to L_{IR} and then use the local Kennicutt (1998) relation to convert L_{IR} to SFR. Using the templates and code from Chary & Elbaz (2001) to fit the 24 μ m flux, assuming $z = 2.7$, we derive a best-fit $L_{\text{IR}} = 5 \times 10^{11} (\mu_A/25)^{-1} L_\odot$. The corresponding implied SFR is $\sim 90 (\mu_A/25)^{-1} M_\odot \text{ yr}^{-1}$. As a consistency check, we also derive the rest-frame 8 μ m luminosity and convert to L_{IR} using $L_{8\mu\text{m}}/L_{\text{IR}} = 10$, consistent with recent results from Rigby et al. (2008) based upon a combination of local and $z \sim 2$ galaxies. To derive the rest-frame 8 μ m we use the same spectral index correction ($\alpha = 2.296$) as in Dey et al. (2008).

¹⁰ As noted by Maraston et al. (2006), templates that include the contribution of TP-AGB stars to the spectrum can yield stellar masses roughly a factor of 2 lower. These templates are not currently implemented in *kcorrect*.

This approach yields a qualitatively consistent total luminosity, $L_{\text{IR}} \sim 3 \times 10^{11} (\mu_{\text{A}}/25)^{-1} L_{\odot}$.

In Figure 4 we overlay the best-fit Chary & Elbaz (2001) template for image B, redshifted to $z = 2.7$, at wavelengths redward of $10 \mu\text{m}$. If the magnification is a factor of 2 lower than our canonical value, which bootstrap simulations indicate is the maximum by which we may be overestimating μ_{A} , this galaxy would lie at the borderline between LIRG and ULIRG luminosity. From their AzTEC millimeter data, Wilson et al. (2008a) also estimate $L_{\text{IR}} = 10^{11} - 10^{12} L_{\odot}$ for this source. The estimated specific star formation rate for this galaxy, $\approx 5 \text{ Gyr}^{-1}$, is comparable to that of similar mass BM/BX galaxies at $z = 1.5 - 2.6$ (Reddy et al. 2006).

4. DISCUSSION

We have presented confirmation observations for a multiply imaged source behind the Bullet Cluster, and identified a third, previously unknown image. From our multiwavelength imaging we argue that the source is most consistent with being a dusty ($A_V \sim 3.3$), strongly star forming galaxy at $z \sim 2.7$. At this redshift our mass model for the cluster core indicates that the galaxy is highly magnified ($\mu_{\text{A}} \sim 25$), implying a large intrinsic stellar mass of $M_{\star} \sim 2 \times 10^{10} M_{\odot}$. We estimate a SFR of $\sim 90 M_{\odot} \text{ yr}^{-1}$ based upon the observed flux in the $24 \mu\text{m}$ band, which we assume to be dominated by emission from redshifted PAH features.

The estimated intrinsic IR luminosity of this galaxy ($5 \times 10^{11} L_{\odot}$) qualifies it as a LIRG, fainter than the ULIRGs typically studied at this epoch. The galaxy is also known to be an exceptionally bright SMG (13.5 mJy at 1.1 mm; Wilson et al. 2008a), and thus may be an ideal system for studying the connection between different classes of IR sources at lower intrinsic luminosity than has previously been possible for this epoch. We anticipate that the galaxy will be detected in scheduled deep *HST* NICMOS observations, providing information on the spatial extent of the lensed images.

The Bullet Cluster, due to its large lensing cross-section, provides an optimal environment in which to identify lensed galaxies such as that presented here. However, even in this rare, massive cluster merger, we detected only one lensed LIRG. This result highlights that the prospects are not good for finding large samples of $z \sim 2$, gravitationally lensed LIRGS. It is for this reason that each case must be highlighted and exploited.

A.H.G. thanks R.-R. Chary, A. Dey, J.-P. Kneib, A. Pope, and G. Wilson for constructive discussions related to this work, S. Charlot and G. Bruzual for providing access to the Charlot & Bruzual (2007) models, and the anonymous referee for comments that significantly improved the manuscript. The authors acknowledge support for this work from NASA/*HST* grants HST-GO-10200, HST-GO-10863, and HST-GO-11099, as well as NASA/*Spitzer* grant 1319141. M.B. also acknowledges support from NASA through Hubble Fellowship grant # HST-HF-01206.01 awarded by the Space Telescope Science Institute.

Facilities: *HST* (ACS), *Spitzer* (IRAC, MIPS), CXO (ACIS), *Magellan*: Baade (PANIC).

REFERENCES

- Barnby, P., et al. 2006, *ApJ*, **642**, 126
- Bertelli, G., Bressan, A., Chiosi, C., Fagotto, F., & Nasi, E. 1994, *A&AS*, **106**, 275
- Blanton, M. R., & Roweis, S. 2007, *AJ*, **133**, 734
- Bolzonella, M., Miralles, J.-M., & Pelló, R. 2000, *A&A*, **363**, 476
- Bradač, M., et al. 2006, *ApJ*, **652**, 937
- Bruzual, A. G. 2007, in IAU Symposium 241, ed. A. Vazdekis & R. F. Peletier (Dordrecht: Kluwer), 125
- Bruzual, G., & Charlot, S. 2003, *MNRAS*, **344**, 1000
- Calzetti, D. 2008, arXiv:0801.2558
- Calzetti, D., Armus, L., Bohlin, R. C., Kinney, A. L., Koornneef, J., & Storchi-Bergmann, T. 2000, *ApJ*, **533**, 682
- Caputi, K. I., et al. 2006, *ApJ*, **637**, 727
- Chabrier, G. 2003, *PASP*, **115**, 763
- Chary, R., & Elbaz, D. 2001, *ApJ*, **556**, 562
- Clowe, D., Bradač, M., Gonzalez, A. H., Markevitch, M., Randall, S. W., Jones, C., & Zaritsky, D. 2006, *ApJ*, **648**, L109
- Clowe, D., Gonzalez, A., & Markevitch, M. 2004, *ApJ*, **604**, 596
- Daddi, E., et al. 2005, *ApJ*, **631**, L13
- Dey, A., et al. 2008, *ApJ*, **677**, 943
- Dickinson, M., Papovich, C., Ferguson, H. C., & Budavári, T. 2003, *ApJ*, **587**, 25
- Dye, S., et al. 2008, *MNRAS*, **386**, 1107
- Fazio, G. G., et al. 2004, *ApJS*, **154**, 10
- Ford, H. C., et al. 2003, in Proc. SPIE 4854, Future EUV/UV and Visible Space Astrophysics Missions and Instrumentation, ed. J. Chris Blades & O. H. W. Siegmund (Bellingham, WA: SPIE), 81
- Gilliland, R. L., & Riess, A. 2002, *The 2002 HST Calibration Workshop: Hubble after the Installation of the ACS and the NICMOS Cooling System* ed. S. Arribas, A. Koekemoer, & B. Whitmore (Baltimore, MD: STScI), 61
- Kennicutt, R. C. Jr., 1998, *ApJ*, **498**, 541
- Knudsen, K. K., van der Werf, P. P., & Kneib, J.-P. 2008, *MNRAS*, **384**, 1611
- Koekemoer, A. M., Fruchter, A. S., Hook, R. N., & Hack, W. 2002, in *The 2002 HST Calibration Workshop: Hubble after the Installation of the ACS and the NICMOS Cooling System*, ed. S. Arribas, A. Koekemoer, & B. Whitmore (Baltimore, MD: STScI), 337
- Krabbe, A., Böker, T., & Maiolino, R. 2001, *ApJ*, **557**, 626
- Le Floch, E., et al. 2005, *ApJ*, **632**, 169
- Lilly, S. J., Le Fevre, O., Hammer, F., & Crampton, D. 1996, *ApJ*, **460**, L1
- Madau, P., Ferguson, H. C., Dickinson, M. E., Giavalisco, M., Steidel, C. C., & Fruchter, A. 1996, *MNRAS*, **283**, 1388
- Makovoz, D., & Marleau, F. R. 2005, *PASP*, **117**, 1113
- Makovoz, D., Moshir, M., Laher, R., & Marsh, K. 2002, in ASP. Conf. Ser. 281, *Astronomical Data Analysis Software and Systems XI*, ed. D. A. Bohlender, D. Durand, & T. H. Handley (San Francisco, CA: ASP), 417
- Makovoz, D., Roby, T., Khan, I., & Booth, H. 2006, in Proc. SPIE 6274, *Advanced Software and Control for Astronomy*, ed. L. Hilton & B. Alan (Bellingham, WA: SPIE), 62740C
- Maraston, C., Daddi, E., Renzini, A., Cimatti, A., Dickinson, M., Papovich, C., Pasquali, A., & Pirzkal, N. 2006, *ApJ*, **652**, 85
- Markevitch, M., Gonzalez, A. H., Clowe, D., Vikhlinin, A., Forman, W., Jones, C., Murray, S., & Tucker, W. 2004, *ApJ*, **606**, 819
- Markevitch, M., Gonzalez, A. H., David, L., Vikhlinin, A., Murray, S., Forman, W., Jones, C., & Tucker, W. 2002, *ApJ*, **567**, L27
- Martini, P., Persson, S. E., Murphy, D. C., Birk, C., Shectman, S. A., Gunnels, S. M., & Koch, E. 2004, in Proc. SPIE 5492, ed. A. F. M. Moorwood & I. Masanori (Bellingham, WA: SPIE), 1653–1660
- Peng, C. Y., Ho, L. C., Impey, C. D., & Rix, H.-W. 2002, *AJ*, **124**, 266
- Pérez-González, P. G., et al. 2005, *ApJ*, **630**, 82
- Pope, A., et al. 2008, *ApJ*, **675**, 1171
- Randall, S. W., Markevitch, M., Clowe, D., Gonzalez, A. H., & Bradač, M. 2008, *ApJ*, **679**, 1173
- Reddy, N. A., & Steidel, C. C. 2004, *ApJ*, **603**, L13
- Reddy, N. A., Steidel, C. C., Fadda, D., Yan, L., Pettini, M., Shapley, A. E., Erb, D. K., & Adelberger, K. L. 2006, *ApJ*, **644**, 792
- Reddy, N. A., Steidel, C. C., Pettini, M., Adelberger, K. L., Shapley, A. E., Erb, D. K., & Dickinson, M. 2008, *ApJ*, **175**, 48
- Rieke, G. H., et al. 2004, *ApJS*, **154**, 25
- Rigby, J. R., et al. 2008, *ApJ*, **675**, 262
- Rudnick, G., et al. 2003, *ApJ*, **599**, 847
- Skrutskie, M. F., et al. 2006, *AJ*, **131**, 1163
- Valiante, E., Lutz, D., Sturm, E., Genzel, R., Tacconi, L. J., Lehnert, M. D., & Baker, A. J. 2007, *ApJ*, **660**, 1060
- Wilkins, S. M., Trentham, N., & Hopkins, A. M. 2008, *MNRAS*, **385**, 687
- Wilson, G. W., et al. 2008a, *MNRAS*, **390**, 1061
- Wilson, G. W., et al. 2008b, *MNRAS*, **386**, 807
- Yan, L., et al. 2005, *ApJ*, **628**, 604